Supplementary Information

Integration of high strength, flexibility, and room-temperature plasticity in ceramic nanofibers

Siyu Qiang[1], Fan Wu[2], Hualei Liu[2], Sijuan Zeng[1], Shuyu Liu[3], Jin Dai[1], Xiaohua Zhang[3], Jianyong Yu[3], Yi-Tao Liu[1,3]*, and Bin Ding[1,2,3]*

[1]State Key Laboratory for Modification of Chemical Fibers and Polymer Materials, College of Textiles, Donghua University, Shanghai 201620, China.
[2]School of Materials Science and Engineering, Shanghai University of Engineering Science, Shanghai 201620, China.
[3]Innovation Center for Textile Science and Technology, Donghua University, Shanghai 200051, China.

* Corresponding authors: liu-yt03@dhu.edu.cn; binding@dhu.edu.cn

This Supplementary Information includes:

Supplementary Figs. 1-25

Supplementary Table 1

Supplementary Figures

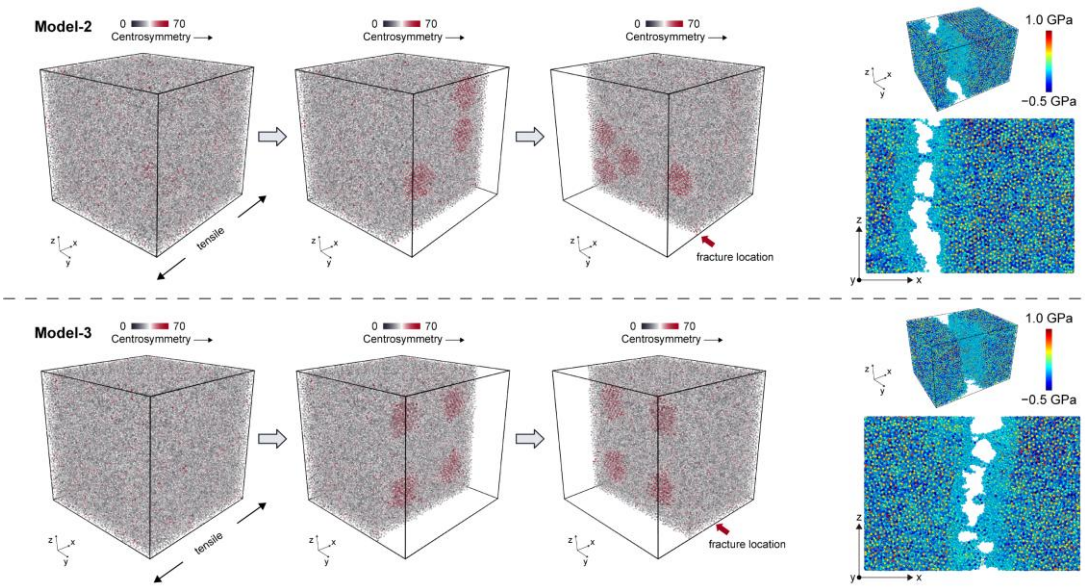

Supplementary Fig. 1 Molecular dynamics (MD) models and tensile simulation details. Structural representations of Model-2 and Model-3, including sliced views to reveal internal details, were used for tensile simulations along the x-axis, providing additional and expanded information to Fig. 1f and 1g. The color scale bar represents the centrosymmetry parameter of each atom in the simulated system.

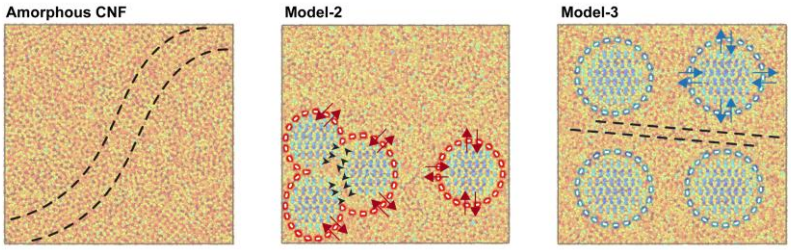

Supplementary Fig. 2 Mechanism analysis of ceramic nanofiber (CNF) deformation. Amorphous CNFs, Model-2, and Model-3 possess exhibit distinct deformation behaviors and mechanisms under tensile loading. Shear-band sliding would dominate the deformation characteristics of amorphous CNFs[1, 2]. In contrast, for Model-2 and Model-3, the synergy of dual-phase structures could contributes to their high strength and toughness during the initial deformation stage[3].

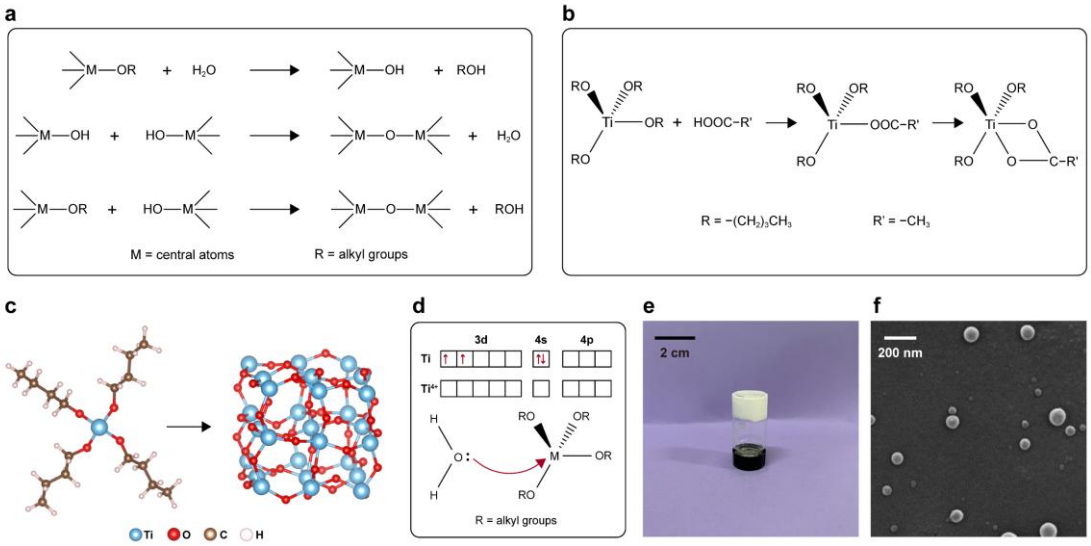

Supplementary Fig. 3 Molecular properties of monomers. **a** Basic chemical reactions in the sol-gel process. The polycondensation of metal alkoxides involves hydrolysis and condensation stages, where H_2O and M−OH act as nucleophiles, respectively. **b** Basic chemical reactions in the ligand-exchange route. The spontaneous exothermic reaction between acetic acid (HOAc, multidentate ligand) and titanium butoxide (TBT, active monomer) is illustrated. **c** Formation of three-dimensional (3D) molecular networks from Ti alkoxides. Most metal alkoxides such as Ti alkoxides, exhibit polyfunctionality and extremely high reactivity. Without deliberate control of the hydrolysis-condensation process, these monomers readily form highly cross-linked and irreversible 3D Ti−O molecular networks. However, this feature can be utilized to prepare spherical particle sol with appropriate process adjustments. **d** Nucleophilic attack facilitated by the electronic state of central atoms. Hydrolysis and condensation of metal alkoxides are fundamentally nucleophilic reactions. The empty orbitals and expandable coordination number of the central Ti atom facilitate attacks by nucleophiles with lone-pair electrons. **e** Optical image of irreversible and rapid gelation during Ti sol synthesis. Gelation occurred rapidly when using previously reported methods[4, 5]. **f** Electrospraying phenomenon observed before gelation. Before gelation, the sol solution was carefully tested for electrospinning, but the electrospraying phenomenon was observed instead. The electrospinning parameters were: electrostatic field = 15 kV, 25 ± 2 °C and 40 ± 2% RH, and 15 cm between the needle tip and collector. The field emission scanning electron microscopy image of the resulting products is shown.

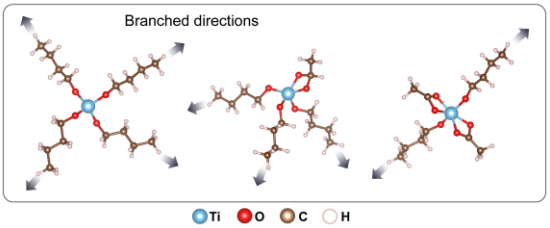

Supplementary Fig. 4 Branching trends of monomers with different coordinated structures. As mentioned before, pristine monomers are prone to branching during the hydrolysis-condensation process. In contrast, modified monomers exhibit limited functionalities and reduced branching behavior owing to enhanced electronegativity and steric hindrance.

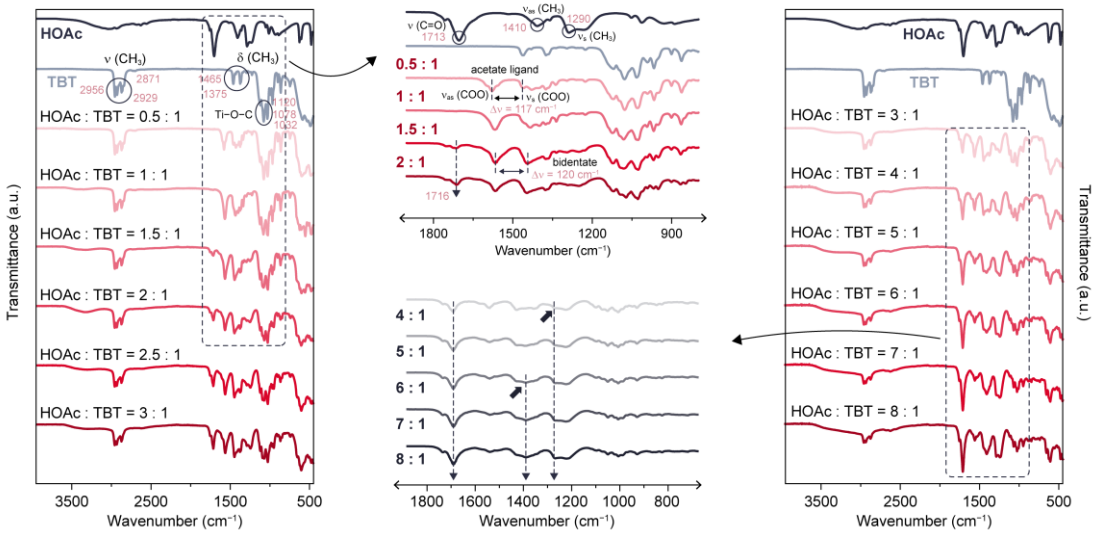

Supplementary Fig. 5 Investigation of the ligand-exchange route using Fourier transform infrared spectroscopy (FTIR) spectra, providing plane curve and expanded information to Fig. 2b. FTIR spectra of products obtained from the coordination reaction between ligands (acetic acid, HOAc) and monomers (titanium butoxide, TBT) at different molar ratios (r_m, ranging from 0.5 to 8.0) are presented. Key characteristic peaks include[6]: ν(C=O) at ~1713 cm^{-1}, $\nu_{as}(CH_3)$ ~1410 cm^{-1}, $\nu_s(CH_3)$ at ~1290 cm^{-1}, $\delta(CH_3)$ at ~1465 and ~1375 cm^{-1}, Ti–O–C at ~1120 cm^{-1}, ~1078 cm^{-1}, and ~1032 cm^{-1}.

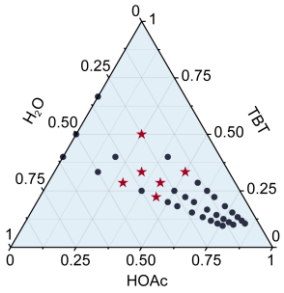

Supplementary Fig. 6 Spinnability of the titanium butoxide - acetic acid - water (TBT-HOAc-H_2O) sol system. The ligand-exchange route effectively limits the reactivity of metal alkoxides. However, an excessively high molar ratios would completely terminate the subsequent reactions of the modified monomers. To optimize the modification scheme, the spinnability of the resulting sols was evaluated, with red stars indicating spinnability and black circles indicating no spinnability.

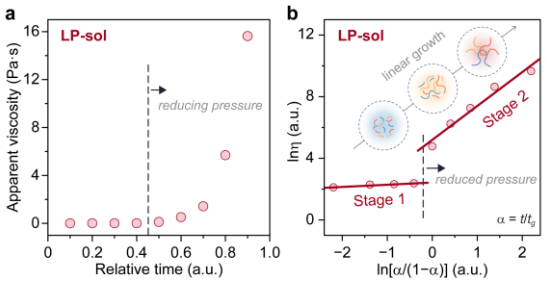

Supplementary Fig. 7 Rheological evolution during the synthesis of linear particle sol (LP-sol). **a** Rheological evolution of LP-sol during synthesis, showing the apparent viscosity (η) as a function of relative time (t/t_g) during the polycondensation of modified monomers (molecular ratio is 1.5) for synthesizing spinnable LP-sol. Here, t is the reaction time, and t_g is the gelation time. **b** Plot of $\ln(\eta)$ as a function of $\ln[(t/t_g)/(1-t/t_g)]$ (here the unit of η is 'mPa s'), highlighting two distinct stages in the LP-sol synthesis process. Inset: illustration depicting the linear growth of modified monomers in LP-sol.

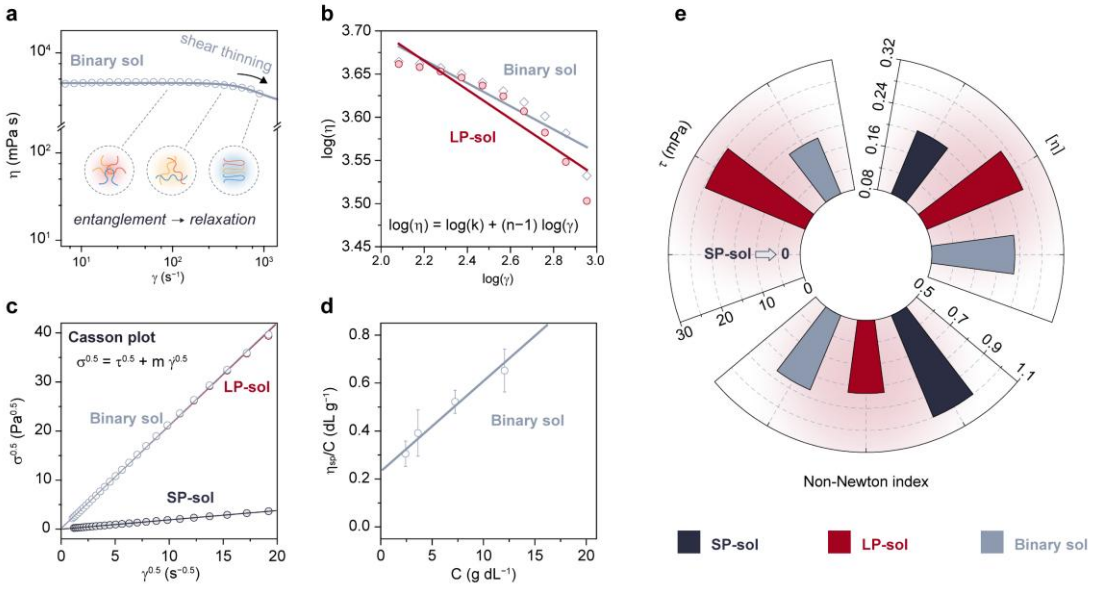

Supplementary Fig. 8 Key rheological properties. **a** Dynamic rheology of the spinnable binary sol. Apparent viscosity (η) as a function of shear rate (γ), showing shear thinning behavior, which suggests the entanglement-relaxation behavior of dispersion particles. **b** Non-Newtonian (Power-law) index calculations. The Power-law index (n) for linear particle sol (LP-sol, relative time that t/t_g=0.8) and binary sol are derived by plotting the logarithm of apparent η against the logarithm of γ. Note that n for spherical particle sol (SP-sol) reaches ~1.0. **c** Casson plots of SP-sol, LP-sol (t/t_g=0.8), and binary sol. Yield stress (τ) values for the sols are calculated from the Casson plots, where the m is a constant. **d** Reduced viscosity (η_{sp}/C) as a function of concentration (C) for binary sol. Intrinsic viscosity ([η]) is extracted by plotting the relation between η_{sp}/C and C for the binary sol. **e** Key rheological parameters, including n, τ, and [η] for SP-sol, LP-sol (t/t_g=0.8), and binary sol.

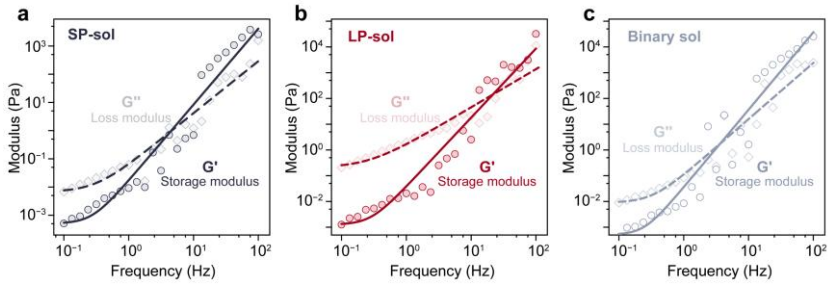

Supplementary Fig. 9 Comparison of storage modulus (*G'*) and loss modulus (*G''*). The relationship between frequency and modulus for **a** spherical particle sol (SP-sol), **b** linear particle sol (LP-sol, relative time is 0.8), and **c** binary sol. Differences in their viscoelastic properties are highlighted, which significantly influence the deformation behavior of charged jets in the electrostatic field.

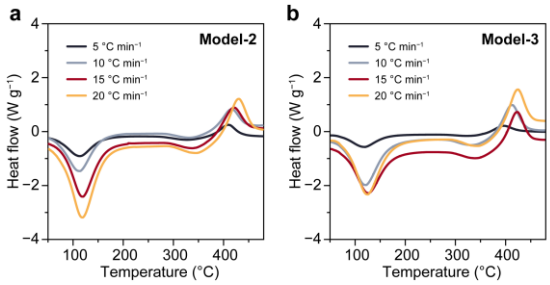

Supplementary Fig. 10 Calculations of the activation energy (ΔG_a) for the amorphous-to-crystallization transition. Gradient non-isothermal differential scanning calorimetry curves for **a** Model-2 and **b** Model-3. The heating rates used are 5 °C min^{-1}, 10 °C min^{-1}, 15 °C min^{-1}, and 20 °C min^{-1}.

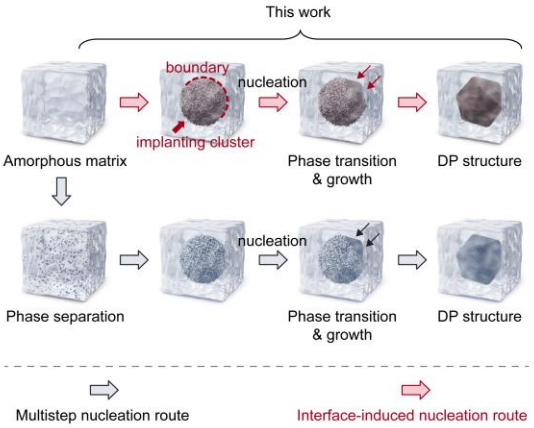

Supplementary Fig. 11 Schematic diagram of the nucleation-growth process, providing additional and expanded information to Fig. 2e and 2h. The nanograins within the disordered matrix follow the multistep nucleation route and the interface-induced nucleation route, respectively.

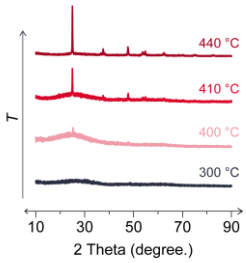

Supplementary Fig. 12 X-ray diffraction patterns of phase structure evolution of the precursor for Model-2.

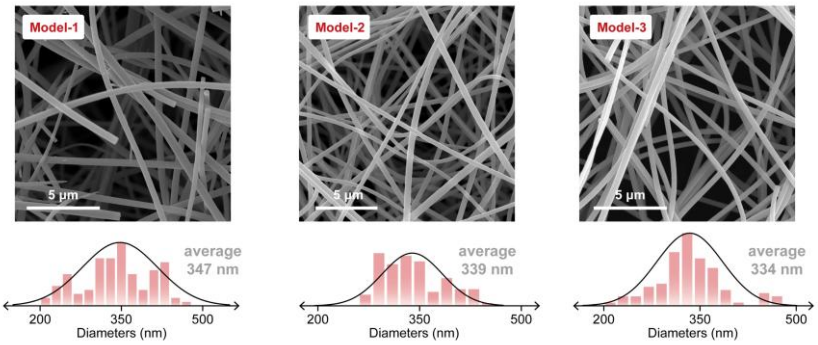

Supplementary Fig. 13 Morphology of ceramic nanofibers obtained from different sols. Scanning electron microscopy images and diameter statistics of dual-phase TiO_2 nanofibers fabricated from spherical particle sol, linear particle sol, and binary sol are presented for comprehensive comparison, labeled as Model-1, Model-2, and Model-3. Their diameters were regulated to exclude size-dependent interference.

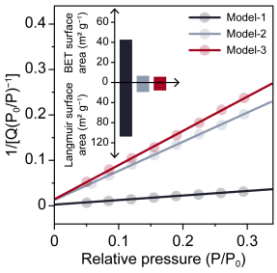

Supplementary Fig. 14 Porosity analysis. Brunauer-Emmett-Teller (BET) surface area calculation plots for Model-1, Model-2, and Model-3. Inset: comparison of BET and Langmuir surface area values.

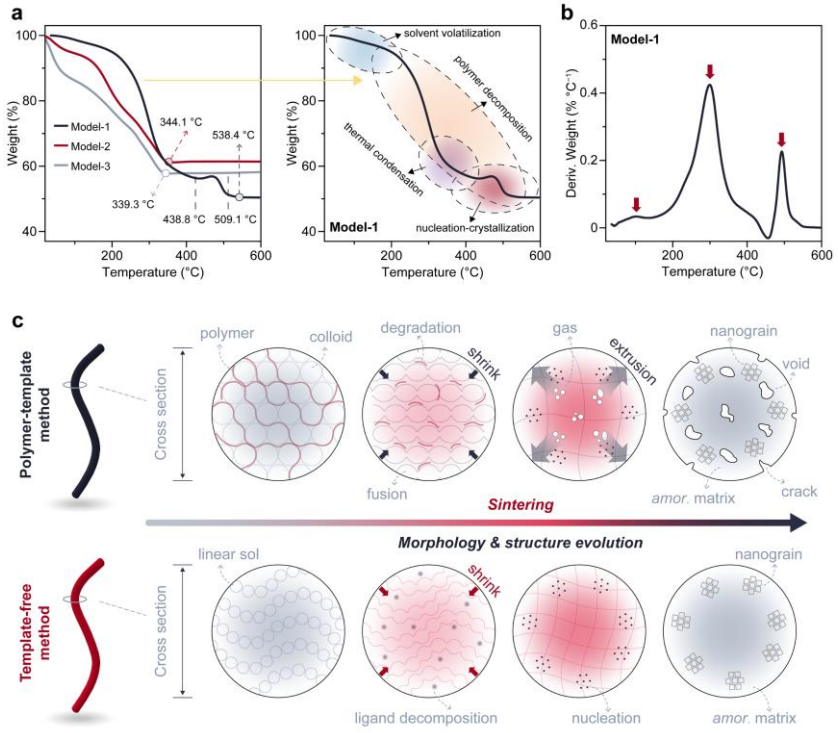

Supplementary Fig. 15 Thermogravimetric analysis (TGA) of Model-1, Model-2, and Model-3 during sintering. **a** TGA curves of Model-1, Model-2, and Model-3. The weight loss of Model-1, including solvent volatilization, thermal condensation, polymer decomposition, and nucleation-crystallization processes. **b** The first-order derivative of the TGA curve for Model-1. **c** Structural evolution of ceramic nanofiber (CNF) fabricated via polymer-template and template-free methods during the sintering process. The weight loss of Model-1 up to ~200 °C is primarily attributed to the evaporation of solvents such as ethanol, butanol, and water. Butanol generated from the hydrolysis of Ti alkoxide (–Ti–OBu + H_2O → –Ti–OH + BuOH). A minor mass loss peak at ~105 °C in the DTG curve reflects the rapid escape of solvents, as these molecules are deeply embedded in the precursor fibers and interact with the polymer and Ti–O crosslinked network, requiring higher temperatures for removal. Another notable mass loss peak appears between 200-400 °C, mainly due to the thermal decomposition of the polyvinylpyrrolidone template, which involves the breaking of polymer chains and their decomposition into small molecules[7]. Organic residues often remain at this stage. A shoulder peak at ~350 °C indicates thermal polycondensation, where retained –Ti–OH groups condense (–Ti–OH + –Ti–OH → –Ti–O–Ti– + H_2O), causing further mass loss. After ~370 °C, nucleation and crystallization commence, while residual carbon undergoes oxidation and releases gases (439-509 °C), leaving diffusion pathways that subsequently form structural defects in the CNFs.

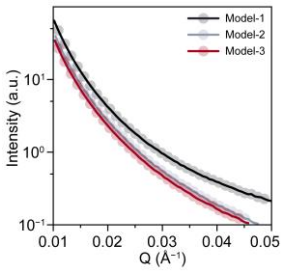

Supplementary Fig. 16 Small-angle X-ray scattering intensity curves for Model-1, Model-2, and Model-3.

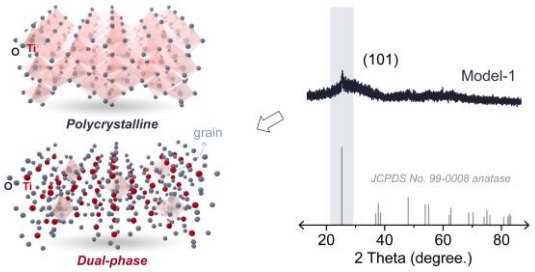

Supplementary Fig. 17 Illustrations comparing crystalline and dual-phase TiO_2 structures highlight the partial crystallization and amorphous matrix characteristic of the latter. X-ray diffraction patterns for Model-1 and crystalline TiO_2 nanofiber counterparts both exhibit a sharp peak at ~25.5°, corresponding to the (101) plane of anatase.

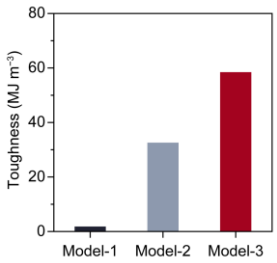

Supplementary Fig. 18 Comparison of toughness. The toughness of Model-3 is dramatically enhanced (~58.45 MJ m^{-3}), which is ~32.11 times and ~1.79 times higher than those of Model-1 and Model-2, respectively.

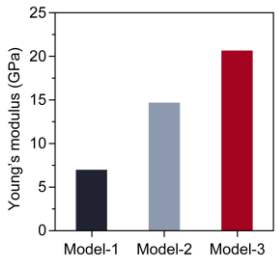

Supplementary Fig. 19 Comparison of Young's modulus. The dense structure and optimized grain distribution render the Young's modulus of Model-3 (~20.66 GPa) higher than that of Model-1 and Model-2.

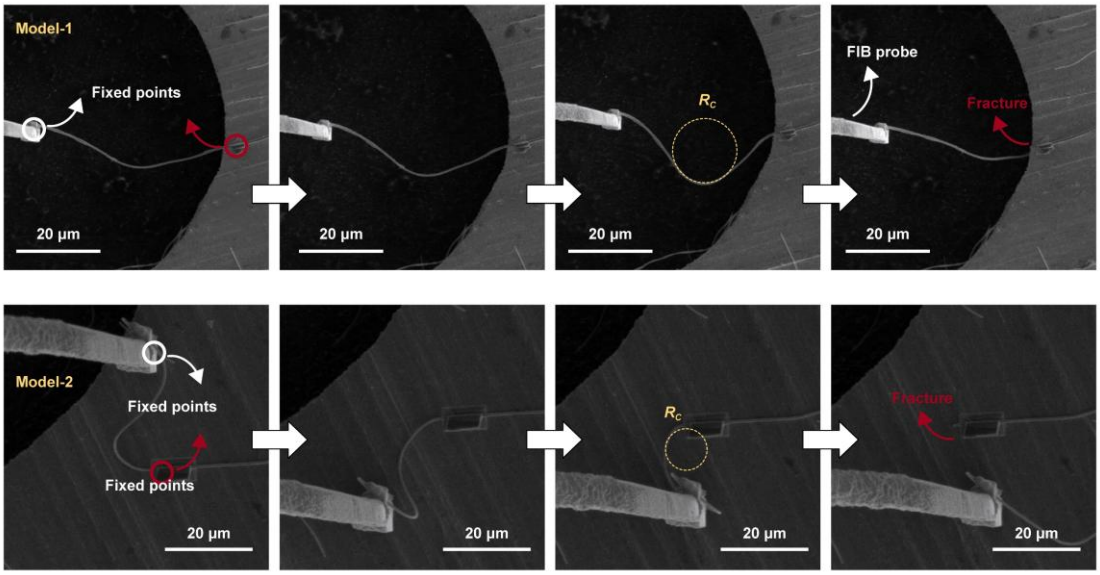

Supplementary Fig. 20 In-situ bending tests. The flexibility of single ceramic nanofiber is assessed by determining the radius of curvature (R_c). The manipulation process involves fixing one end of a nanofiber to a substrate while attaching the other to a movable probe, then bending it to determine the lowest R_c for Model-1 and Model-2.

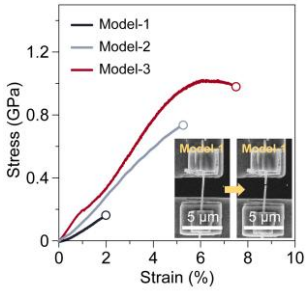

Supplementary Fig. 21 Stress-strain curves of experimental samples corresponding to the three models were successfully reproduced. While minor deviations in absolute values may result from experimental errors and slight variations between samples batches, it is noteworthy that the replications are highly consistent with the conclusions of the manuscript, both in terms of mechanical behaviors and overall trends.

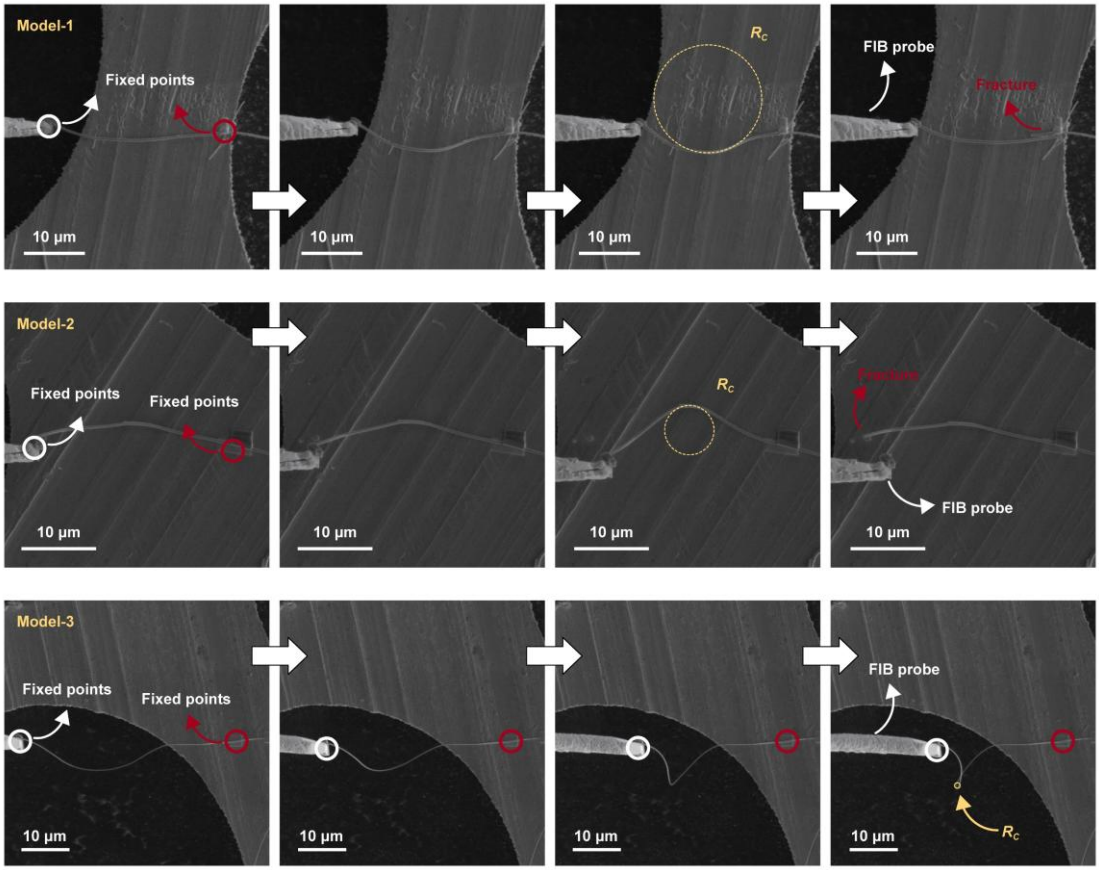

Supplementary Fig. 22 The flexible features of experimental samples corresponding to the three models were successfully reproduced.

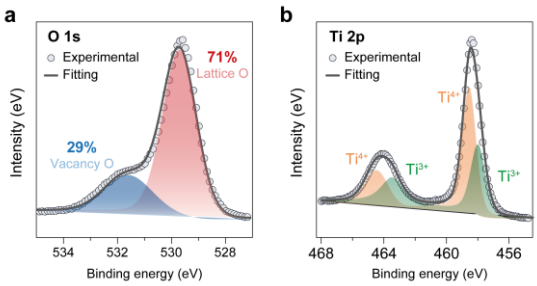

Supplementary Fig. 23 X-ray photoelectron spectroscopy analysis of the O 1*s* and Ti 2*p* spectra for the dual-phase structure (Model-2).

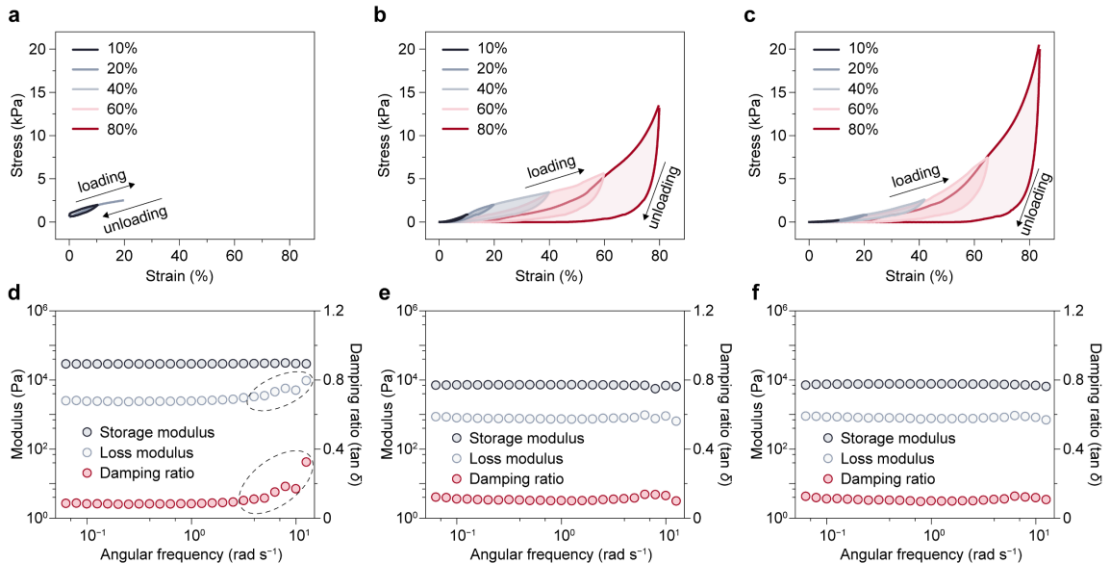

Supplementary Fig. 24 The synthesized Model-1, Model-2, and Model-3 were assembled into fibrous aerogels (MA), and the dynamic mechanical properties of these aggregates were evaluated. **a–c** Curves showing the strength (σ) as a function of compressive strain (ε) for the aerogel samples composed of Model-1, Model-2, and Model-3, respectively. **d–f** Frequency dependence of the storage modulus, loss modulus, and damping ratio of the aerogel samples consisting of Model-1, Model-2, and Model-3, respectively, under an oscillatory ε of 3%. Compared to MA-1, MA-2 and MA-3 exhibited robust mechanical properties and could withstand large compressive loads, with ε up to ~80%. In contrast, MA-1 cracked and collapsed after experiencing a compressive ε of only ~20%. The mechanical differences between the aggregates and the single nanofiber showed high consistency. When comparing MA-2 and MA-3, it was observed that MA-3 demonstrated superior σ at the same ε, particularly at ε ~80%, where its σ reached ~20.4 kPa. Furthermore, MA-3 exhibited consistent storage and loss moduli over three orders of magnitude in angular frequency. Its damping ratio remained more stable than those of MA-1 and MA-2 at high frequencies. The preparation of these fibrous aerogels was accomplished using the freeze-template method[8]. First, nanofibers were dispersed in an aqueous solution and further processed using a high-pressure homogenizer. Subsequently, prepared silica sol binders were added to the dispersion and thoroughly stirred to ensure homogeneity. The silica sol binders were formulated with a molar ratio of tetraethyl silicate: ethanol: water: phosphoric acid at 1:45:46:0.002. The homogenized nanofiber dispersions were then frozen and freeze-dried for 24 h. Finally, the aggregates were sintered below the formation temperature of the hypocrystalline structure (~380 °C).

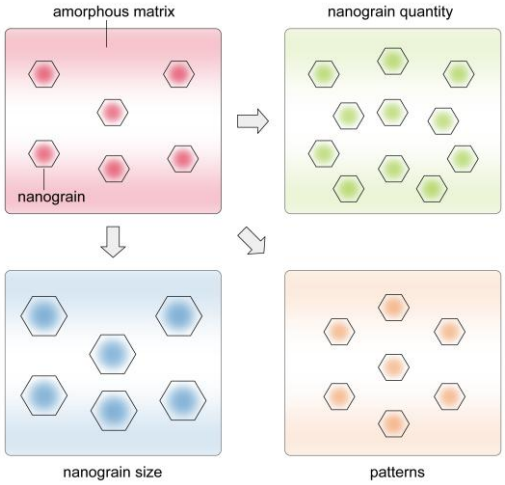

Supplementary Fig. 25 Promising directions for further improving the comprehensive mechanical properties of dual-phase ceramic nanofibers.

Supplementary Table

Supplementary Table 1 Spinnability evaluations of the binary sols, which obtained by combining spherical particle sol (SP-sol) and linear particle sol (LP-sol). The parameters employed are as follows: static voltages ranging from 5-45 kV, environmental temperatures ranging from 15-30°C, relative humidities ranging from 20%-60%, and distances ranging from 10-30 cm between the needle tip and the collector.

Composition of binary sol		Spinnability	Product morphology
SP-sol	LP-sol		
1 wt%	99 wt%	electrospinning	nanofibers
2 wt%	98 wt%	electrospinning	nanofibers
3 wt%	97 wt%	electrospinning	nanofibers
4 wt%	96 wt%	electrospinning	nanofibers
5 wt%	95 wt%	electrospinning	nanofibers
6 wt%	94 wt%	electrospinning	nanofibers with necks
7 wt%	93 wt%	electrospinning/spraying	nanofibers and particles
8 wt%	92 wt%	electrospraying	nanoparticles
9 wt%	91 wt%	electrospraying	nanoparticles
10 wt%	90 wt%	electrospraying	nanoparticles

Supplementary References

1. Zhao Y*, et al.* Dual phase nano-particulate AlN composite - a kind of ceramics with high strength and ductility. *Ceram. Int.* **45**, 19845 (2019).

2. Li F*, et al.* Dual-phase super-strong and elastic ceramic. *ACS Nano* **13**, 4191 (2019).

3. Guo J*, et al.* Hypocrystalline ceramic aerogels for thermal insulation at extreme conditions. *Nature* **606**, 909 (2022).

4. Liu C*, et al.* High toughness combined with high strength in oxide ceramic nanofibers. *Adv. Mater.* **35**, 2304401 (2023).

5. Xu Z*, et al.* Inhibited grain growth through phase transition modulation enables excellent mechanical properties in oxide ceramic nanofibers up to 1700 °C. *Adv. Mater.* **35**, 2305336 (2023).

6. Doeuff S, Henry M, Sanchez C, Livage J. Hydrolysis of titanium alkoxides: modification of the molecular precursor by acetic acid. *J. Non-Cryst. Solids* **89**, 206 (1987).

7. Zhang Y*, et al.* Superior flexibility in oxide ceramic crystal nanofibers. *Adv. Mater.* **33**, 2105011 (2021).

8. Si Y, Wang X, Dou L, Yu J, Ding B. Ultralight and fire-resistant ceramic nanofibrous aerogels with temperature-invariant superelasticity. *Sci. Adv.* **4**, eaas8925 (2018).